Modeling of ultrabroadband and single-cycle phenomena in anisotropic quadratic crystals

Matteo Conforti, Fabio Baronio, Costantino de Angelis

Modelling of ultrabroadband and single-cycle phenomena in anisotropic quadratic crystals

Matteo Conforti,[1] Fabio Baronio,[1] and Costantino De Angelis[1]

[1]*CNISM, Dipartimento di Ingegneria dell'Informazione, Università di Brescia, Via Branze 38, 25123 Brescia, Italy*

Corresponding author: matteo.conforti@ing.unibs.it

We present a comprehensive model to describe the propagation of single-cycle and broadband optical pulses in anisotropic, dispersive and nonlinear materials. Two nonlinear coupled wave equations describe the dynamics and interactions of optical pulses in uniaxial second-order nonlinear materials. The equations are first order in the propagation coordinate and are valid for arbitrarily wide pulse bandwidth, providing an accurate modeling of the evolution of ultra-broadband pulses also when the separation into different coupled frequency components is not possible or not profitable. We exploit this model to simulate recently observed femtosecond single-cycle multiterahertz transients in gallium selenide and to predict harmonic generation and spectral broadening in the visible and mid-infrared in lithium niobate.

OCIS codes: 190.2620, 190.4223, 320.2250.

1. Introduction

Femtosecond light pulses play an important role in the study of ultrafast dynamics of elementary excitations in molecules and solids [1, 2], and in exploring new regimes of light matter interactions [3]. Structural changes in molecules or in molecular complexes were monitored directly in the time domain by means of the transient absorption of molecular vibrations [4]. Vibrational dynamics in liquids or in proteins have been succesfully studied with femtosecond pulses in the mid-infrared [5, 6]. Femtosecond infrared spectroscopy has also **been** applied to problems in solid state physics.

In the last decade, considerable efforts have been dedicated to the achievement of shorter femtosecond light pulses, to improve temporal resolution, and to expand the frequency tunability of pulses [7, 8]. In this context, different schemes based on parametric frequency conversion in uniaxial quadratic crystals have been used to generate tunable high intensity femtosecond pulses in the ultraviolet, visible, near and mid infrared: as representative examples, ultrabroadband near infrared self-phase-stabilized pulses by difference-frequency generation in β barium borate [9], single-cycle ultrabroad-band multiterahertz transients in gallium selenide (GaSe) [10], few optical cycle pulses tunable from the visible to the mid infrared by optical parametric amplifiers in β barium borate and periodically poled lithium tantalate [11].

Theoretical research efforts on the modeling of this kind of single-cycle and broadband phenomena are limited. From the theoretical side, the analysis of optical pulse propagation in anisotropic quadratic media typically involves the definition of polarized complex envelopes whose variations are supposed to be slow with respect to the oscillation of carrier frequencies (slowly varying envelope approximation (SVEA) [12]). In the frequency domain, this assumption is equivalent to requiring that the envelope bandwidths are narrow with respect to the carrier frequencies. Moreover when second-order parametric processes are considered, the usual approach is to write coupled equations for the separated frequency bands relevant for the processes [7, 13, 14]. However, when single-cycle or ultrabroadband phenomena take place, the harmonic bands merge, generating a single broad spectrum. Obviously, in these cases, the coupled envelopes description of the propagation fails due the frequency overlapping of the distinct bands. Different works showed that it is possible to model the propagation of fields with pulse duration down to the single optical oscillation cycle and to the generation of very broad spectra [15]–[24].

The scope of this article is to present a model for the description of single-cycle and ultrabroadband electric field phenomena in dispersive quadratic uniaxial media. This model provides a powerful tool for analytical treatment due to its simplicity, and can be easily solved with a modest computational effort. The paper is organized as follows: in section 2 we recall the derivation of the master equations in anisotropic media, discussing the approximations and the limit of validity of the model. In section 3, we test our model analyzing recent experimental results of single-cycle mid-infrared terahertz generation in GaSe crystals [10], finding an excellent agreement between the experimental data and our numerics; moreover we predict harmonic generation and spectral broadening in the mid-infrared and in the visible in Periodically Poled MgO-doped Lithium Niobate (PPMgOLN). Finally, we present our conclusions in Section 4.

2. Derivation of the propagation equations

We start from Maxwell equations written in MKS units, in the reference frame $x'y'z'$

$$\nabla' \times \mathbf{E}' = -\frac{\partial \mathbf{B}'}{\partial t} \tag{1}$$

$$\nabla' \times \mathbf{H}' = \frac{\partial \mathbf{D}'}{\partial t} \tag{2}$$

$$\mathbf{B}' = \mu_0 \mathbf{H}' \tag{3}$$

$$\mathbf{D}' = \varepsilon_0 \mathbf{D}'_L + \mathbf{P}'_{NL} \tag{4}$$

where $\mathbf{D}'_L$ and $\mathbf{P}'_{NL}$ account for the linear and nonlinear response of the medium, respectively. The components of the linear displacement vector for a dispersive anisotropic medium reads (assuming summation over repeated indxes)

$$D'_{L,j} = \int_{-\infty}^{\infty} \varepsilon'_{jk}(t-t') E'_k(t') dt' \,. \tag{5}$$

In the reference frame of the principal axes of **a** uniaxial crystal, the dielectric permittivity tensor is the diagonal matrix $\varepsilon = diag(\varepsilon_o, \varepsilon_o, \varepsilon_e)$, where $\varepsilon_o, \varepsilon_e$ are the ordinary and extraordinary relative dielectric permittivity, respectively. The reference frame of the principal axes of the crystal $(x'y'z')$ is not convenient for the derivation of the propagation equations. We introduce a reference frame xyz that is rotated by (θ, ϕ) with respect to crystal axes. Namely, θ is the angle between the propagation vector (parallel to z) and the crystalline z' axis (the crystal optical axis), and ϕ is the azimuthal angle between the propagation vector and the $x'z'$ crystalline plane. The two reference frame are linked by the orthogonal rotation

matrix A:

$$A = \begin{bmatrix} \cos\phi\cos\theta & \sin\phi\cos\theta & -\sin\theta \\ -\sin\phi & \cos\phi & 0 \\ \sin\theta\cos\phi & \sin\phi\sin\theta & \cos\theta \end{bmatrix}. \tag{6}$$

The dielectric permittivity tensor in the xyz frame is no longer diagonal, and it can be written as

$$\begin{aligned} \varepsilon &= A\varepsilon' A^T \\ &= \begin{bmatrix} \varepsilon_o\cos^2\theta + \varepsilon_e\sin^2\theta & 0 & (\varepsilon_o - \varepsilon_e)\cos\theta\sin\theta \\ 0 & \varepsilon_o & 0 \\ (\varepsilon_o - \varepsilon_e)\cos\theta\sin\theta & 0 & \varepsilon_o\sin^2\theta + \varepsilon_e\cos^2\theta \end{bmatrix}. \end{aligned} \tag{7}$$

In the reference frame xyz, it is possible to decompose the electromagnetic field into two linear and orthogonal polarizations of $\mathbf{D}$, both transverse to the propagation direction z [25]: $\mathbf{D} = (0, D_y, 0)^T + (D_x, 0, 0)^T$. We assume the propagation of plane waves, so the electric field and displacement vectors depend upon the z coordinate (and time) only. It is worth noting that this decomposition is rigorous for linear propagation only, since the nonlinearity can rotate locally the polarization. However it is reasonable to consider the nonlinearity as a perturbative term whose effect is to couple the orthogonal polarized field vector components during propagation. If we neglect dispersion and nonlinearity, just for the moment, the electric field vector can be straightforwardly computed as:

$$\mathbf{E} = \varepsilon_0^{-1}\varepsilon^{-1}\mathbf{D} = \varepsilon_0^{-1}\begin{bmatrix} \left(\frac{\cos^2\theta}{\varepsilon_o} + \frac{\sin^2\theta}{\varepsilon_e}\right) D_x \\ \varepsilon_o^{-1} D_y \\ \frac{\varepsilon_e - \varepsilon_o}{\varepsilon_e\varepsilon_o}\cos\theta\sin\theta D_x \end{bmatrix} \tag{8}$$

By eliminating the magnetic field from Maxwell equations we obtain the vector wave equation:

$$\nabla\times\nabla\times\mathbf{E} - \frac{1}{c^2}\frac{\partial^2\mathbf{D}_L}{\partial t^2} = \frac{1}{\varepsilon_0 c^2}\frac{\partial^2\mathbf{P}_{NL}}{\partial t^2} \tag{9}$$

Note that obviously $\nabla\cdot\mathbf{D} = 0$, but $\nabla\cdot\mathbf{E} \neq 0$. By writing (2equation.2.9) in components we obtain

$$\frac{\partial^2 E_x}{\partial z^2} - \frac{1}{c^2}\frac{\partial^2 D_{L,x}}{\partial t^2} = \frac{1}{\varepsilon_0 c^2}\frac{\partial^2 P_{NL,x}}{\partial t^2} \tag{10}$$

$$\frac{\partial^2 E_y}{\partial z^2} - \frac{1}{c^2}\frac{\partial^2 D_{L,y}}{\partial t^2} = \frac{1}{\varepsilon_0 c^2}\frac{\partial^2 P_{NL,y}}{\partial t^2} \tag{11}$$

$$0 = \frac{1}{\varepsilon_0 c^2}\frac{\partial^2 P_{NL,z}}{\partial t^2} \tag{12}$$

The last equation witnesses the fact that the decomposition into two independent orthogonal polarizations is rigorous only in the linear case. We neglect $P_{NL,z}$, in the reasonable hypothesis of small nonlinearity.

Exploiting the relation (2equation.2.5) we obtain:

$$\begin{aligned}\frac{\partial^2 E_m(z,t)}{\partial z^2} - \frac{1}{c^2}\frac{\partial^2}{\partial t^2}\int_{-\infty}^{+\infty} E_m(z,t')\varepsilon_m(t-t')dt' \\ = \frac{1}{\varepsilon_0 c^2}\frac{\partial^2}{\partial t^2}P_{NL,m}(z,t)\,, \quad m = x,y\end{aligned} \tag{13}$$

where we have defined

$$\varepsilon_x = \left(\frac{\cos^2\theta}{\varepsilon_o} + \frac{\sin^2\theta}{\varepsilon_e}\right)^{-1} \tag{14}$$

$$\varepsilon_y = \varepsilon_o \tag{15}$$

We thus have obtained the propagation equations for an ordinary polarized wave E_y and an extraordinary polarized wave E_x.

By defining the Fourier transform $\mathcal{F}[E](\omega) = \hat{E}(\omega) = \int_{-\infty}^{+\infty} E(t)e^{-i\omega t}dt$, we can write (13equation.2.13) in the frequency domain:

$$\frac{\partial^2 \hat{E}_m(z,\omega)}{\partial z^2} + \frac{\omega^2}{c^2}\hat{\varepsilon}_m(\omega)\hat{E}_m(z,\omega) = -\frac{\omega^2}{\varepsilon_0 c^2}\hat{P}_{NL,m}(z,\omega), \tag{16}$$

where c is the velocity of light in vacuum, ε_0 is the vacuum dielectric permittivity, $\hat{\varepsilon}_m(\omega) = 1 + \hat{\chi}_m(\omega)$, $\hat{\chi}_m(\omega)$ is the linear electric susceptibility and $k_m(\omega) = (\omega/c)\sqrt{\hat{\varepsilon}_m(\omega)}$ is the propagation wavenumber.

We now proceed to obtain from the second order vector wave equation (2equation.2.16) an equation first order in the propagation coordinate z, describing electromagnetic fields propagating in the forward direction only. Several techniques were proposed in literature in order to achieve a pulse propagation equation with minimal assumptions [3, 16–22]. The interested reader can find in [21] an exhaustive discussion on the different derivation styles. Here we decided to follow a simple approach firstly proposed by Brabec and Krausz [3] for describing propagation in isotropic cubic media, and successfully extended to the case of isotropic quadratic media [23, 24]. It is worth noting that, in the case of plane wave propagation we are interested in, all the techniques reported in [3, 16–22] lead to the same model.

We factor out the fast dependence of the propagation coordinate from the electric field, for all the frequencies: $\hat{E}_m(z,\omega) = \hat{U}_m(z,\omega)\exp[-ik_m(\omega)z]$. This definition amounts writing the electric field as the product of a spatial carrier wave and a slowly varying envelope. Since we remove the exact propagation constant at every frequency, we can avoid making any requirement on the bandwidth of the pulses. The wave equation for the field $\hat{U}_m$ reads:

$$\frac{\partial^2 \hat{U}_m(z,\omega)}{\partial z^2} - 2ik_m(\omega)\frac{\partial \hat{U}_m(z,\omega)}{\partial z} = -\frac{\omega^2}{\varepsilon_0 c^2}\hat{P}_{NL,m}(z,\omega)e^{ik_m(\omega)z}. \tag{17}$$

We make the slowly evolving wave approximation (SEWA [3]), that is $|\partial_z \hat{U}_m| << 2k(\omega)|\hat{U}_m|$, and thus we can write

$$\frac{\partial \hat{U}_m(z,\omega)}{\partial z} = -i\frac{\omega^2}{2\varepsilon_0 c^2 k_m(\omega)}\hat{P}_{NL,m}(z,\omega)e^{ik_m(\omega)z}, \tag{18}$$

and from the definition of $\hat{U}_m$, we obtain the equation for the electric field:

$$\frac{\partial \hat{E}_m(z,\omega)}{\partial z} + ik_m(\omega)\hat{E}_m(z,\omega) = -i\frac{\omega}{2\varepsilon_0 c n_m(\omega)}\hat{P}_{NL,m}(z,\omega). \tag{19}$$

We consider an instantaneous second order nonlinear polarization (summation over repeated indexes is assumed)

$$P'_{NL,j} = 2\varepsilon_0 d_{jkl}E'_k E'_l \tag{20}$$

where d_{jkl} is the second order nonlinear susceptivity tensor, that is usually given in the crystal axes reference frame. In order to obtain the effective nonlinearity [26], we have to rotate the polarization vector with matrix A, following the prescription

$$\mathbf{P}_{NL}(\mathbf{E}) = A\mathbf{P}'_{NL}(A^T\mathbf{E}). \tag{21}$$

After some calculations, we can write:

$$\begin{aligned}
\frac{\partial \hat{E}_x}{\partial z} + ik_x(\omega)\hat{E}_x &= \frac{-i\omega}{cn_x(\omega)}\mathcal{F}[2d_1E_xE_y + d_2E_y^2] \\
\frac{\partial \hat{E}_y}{\partial z} + ik_y(\omega)\hat{E}_y &= \frac{-i\omega}{cn_y(\omega)}\mathcal{F}[d_1E_x^2 + 2d_2E_xE_y]
\end{aligned} \tag{22}$$

where d_1 is the effective nonlinearity for oee, eoe and eeo interactions, whereas d_2 is the effective nonlinearity for oeo, eoo and ooe interactions. We have neglected eee (terms proportional to E_x^2 in the first equation) and ooo (terms proportional to E_y^2 in the second equation)

interactions since they are usually not phase matched by birefringence. However they can be added if necessary without any additional complication. We have also neglected the $P_{NL,z}$ component as explained before. The values of the effective nonlinearity depend upon the crystal and their values can be found in several textbooks [27]. In Table 1Effective Nonlinear Coefficients. As to GaSe, $d_{22} = 54pm/V$; as to MgOLN $d_{22} = 0$, $d_{31} = 4.5pm/V$table.1 we report the effective nonlinearity for the crystals we use in the next section.

Equations (22equation.2.22) are first order in the propagation coordinate, conserve the total field energy (see Appendix) and retain their validity for arbitrary wide pulse bandwidth. As opposed to what is reported in the literature [21], we focus our attention on situations where $\hat{E}_x(\omega)$ or/and $\hat{E}_y(\omega)$ are broadband signals extending from a few terahertz to hundreds of terahertz, as observed in several physical settings [10]. For this reason we need here to take full advantage of the approach first introduced in [23, 24] to efficiently tackle broadband $\chi^{(2)}$ interactions. The computational effort needed to solve these equations, by a standard split step Fourier method exploiting Runge-Kutta for the nonlinear step, is of the order of magnitude of that needed for solving the standard three-wave equations universally exploited to describe light propagation in quadratic crystals [28, 29]. However Eqs. (22equation.2.22) are far more general, and are equivalent to Maxwell equations when dealing with unidirectional propagation [17]. In the next section we show some examples of ultra-broadband pulse generation in anisotropic quadratic crystals that cannot be handled by standard three-wave interactions but are well described by model (22equation.2.22).

3. Examples

In this section we report a representative example of modelling single cycle generation in the terahertz domain by optical rectification in GaSe [10], and we predict harmonics generation and spectral broadening in PPMgOLN in the mid-infrared and in the visible.

Single-cycle multiterahertz transients in GaSe

We consider the generation of single-cycle terahertz transients as the idler of a parametric amplifier. This phenomenon has been observed very recently in experiments exploiting GaSe crystals [10]. GaSe is an excellent material for THz generation due to its exceptionally large nonlinear coefficient $d_{22} = 54pm/V$ and infrared transparency. The strong anisotropy allows for widely tunable phase matching. For a given set of pump, signal and idler frequencies $(\omega_p, \omega_s, \omega_i)$ the phase matching condition $\Delta k = k_p - k_s - k_i = 0$ can be satisfied by tuning

the propagation angle θ. In a type-I interaction ($e_p \rightarrow o_s + o_i$) the effective nonlinearity is maximized for an azimuthal angle $\phi = \pi/6$ (see Tab. 1Effective Nonlinear Coefficients. As to GaSe, $d_{22} = 54pm/V$; as to MgOLN $d_{22} = 0$, $d_{31} = 4.5pm/V$table.1). To achieve the broadest phase-matching bandwidth it is necessary to suppress the group velocity mismatch between the signal and the idler and to minimize group velocity dispersion. In order to achieve this condition it is necessary to choose accurately the pump wavelength; as studied in [10] the phase matching bandwidth is maximized for a pump wavelength $\lambda_p = 1.18\mu m$ and a signal wavelength $\lambda_s = 1.28\mu m$. We thus consider an extraordinary polarized gaussian pulse, with $T_p = 115fs$, peak intensity $I_p = 25GW/cm^2$ at λ_p for the pump, which mixes with an ordinary polarized gaussian pulse, with $T_s = 30fs$, peak intensity $I_s = 40GW/cm^2$ at λ_s in a $L = 140\mu m$ long GaSe crystal cut for type-I interaction ($\phi = \pi/6$) with a phase matching angle $\theta = 12.5^o$. Figure 1Generation of single cycle idler pulse by parametric mixing of pump and signal waves centered at 1.18 and 1.28 μm, respectively. $I_p = 25GW/cm^2$, $I_s = 40GW/cm^2$, L=140μm. a) Input (dashed curves) and output (solid curves) power spectrum of extraordinary wave E_x (red curves) and ordinary wave E_y (blue curves). b) Power spectrum of ordinary output THz component. c) Single cycle THz transients obtained by filtering E_y in [1-100] THz range. Dashed curve, in phase pump-signal input; solid curve, phase difference $3/4\pi$figure.1a) shows the power spectrum of the input and output pulses as obtained from numerical solution of Eqs. (22equation.2.22). The THz ordinary idler, generated with an efficiency of 3.5% and shown in linear scale in Fig 1Generation of single cycle idler pulse by parametric mixing of pump and signal waves centered at 1.18 and 1.28 μm, respectively. $I_p = 25GW/cm^2$, $I_s = 40GW/cm^2$, L=140μm. a) Input (dashed curves) and output (solid curves) power spectrum of extraordinary wave E_x (red curves) and ordinary wave E_y (blue curves). b) Power spectrum of ordinary output THz component. c) Single cycle THz transients obtained by filtering E_y in [1-100] THz range. Dashed curve, in phase pump-signal input; solid curve, phase difference $3/4\pi$figure.1b), spans over several octaves from 1 to 60 THz. As secondary effects, we notice an extraordinary THz component generated with much lower efficiency and a consistent spectral broadening of the pump. Figure 1Generation of single cycle idler pulse by parametric mixing of pump and signal waves centered at 1.18 and 1.28 μm, respectively. $I_p = 25GW/cm^2$, $I_s = 40GW/cm^2$, L=140μm. a) Input (dashed curves) and output (solid curves) power spectrum of extraordinary wave E_x (red curves) and ordinary wave E_y (blue curves). b) Power spectrum of ordinary output THz

component. c) Single cycle THz transients obtained by filtering E_y in [1-100] THz range. Dashed curve, in phase pump-signal input; solid curve, phase difference $3/4\pi$figure.1c) shows the ordinary polarized electric field filtered in the [1-100]THz range, showing a FWHM envelope around 50fs, corresponding to a single oscillation of a 20 THz carrier. It is worth noting that our approach enable us to calculate the real electric field: this is of paramount importance in few cycle phenomena, where the carrier-envelope phase (CEP) must be taken into account. In fact, due to dispersion, CEP is strongly sensitive to just a few microns propagation in a solid medium. The CEP can be controlled by varying pump-signal relative phase: in Fig. 1Generation of single cycle idler pulse by parametric mixing of pump and signal waves centered at 1.18 and 1.28 μm, respectively. $I_p = 25GW/cm^2$, $I_s = 40GW/cm^2$, L=140μm. a) Input (dashed curves) and output (solid curves) power spectrum of extraordinary wave E_x (red curves) and ordinary wave E_y (blue curves). b) Power spectrum of ordinary output THz component. c) Single cycle THz transients obtained by filtering E_y in [1-100] THz range. Dashed curve, in phase pump-signal input; solid curve, phase difference $3/4\pi$figure.1c) dashed curve corresponds to in-phase pump-signal input, while solid curve corresponds to a pump and signal relative phase of $3/4\pi$. The numerical results reproduce perfectly the experiments of Ref. [10].

Harmonic generation and spectral broadening in PP-MgOLN

We consider a PPMgOLN crystal, cut for type-I interaction [30, 31]. In PPMgOLN, type-I ($o + o \rightarrow e$) quasi-phase-matched (QPM) scheme, exploiting the $d_{31} = 4.5pm/V$ nonlinear coefficient, offers a spectral range in which the wave-vector mismatch varies more slowly with the fundamental wavelength than in conventional type-0 ($e + e \rightarrow e$) QPM scheme, using the $d_{33} = 25pm/V$ nonlinear coefficient, giving rise to broadband phase-matched nonlinear interactions.

We consider an ordinary polarized (E_y) fundamental frequency (FF) gaussian pulse with a duration $T = 100fs$, centered at $\lambda = 1550nm$, peak intensity $I = 90GW/cm^2$, that propagates in a $L = 6.5mm$ long PPMgOLN sample. The off-diagonal nonlinear coefficient d_{31} is poled with a period $\Lambda = 19.55\mu m$, and the crystal orientation is $\theta = \phi = \pi/2$.

Figure 2Evolution of the total power spectrum (dB). The initial pulse has gaussian shape and the parameters are $T = 100fs$, $\lambda = 1550nm$, $I = 60GW/cm^2$, $\Lambda_{QPM} = 19.55\mu m$, $\theta = \phi = \pi/2$figure.2 shows the evolution of the field spectrum during the propagation. We see a consistent broadening on both the red and blue side of the input field spectrum

at $\lambda_{FF} = 1550nm$ which, at the end of the crystal, reaches 1.5 octave spanning. We see the generation of spectral components at the second harmonic (SH) and third harmonic (TH). The generation of field components at the SH is ruled by mismatched interactions: fig. 4a) Phase-matching curve for type I SHG interaction in a PPMg0LN crystal. b) Level curves of sum frequency wavelength ($\lambda_3 = \lambda_1 + \lambda_2$) and of mismatch $\Delta k = 0$ (thick blue curves) for V-order (superimposed to $\lambda = 540nm$) and VII-order QPM (superimposed to $\lambda = 470nm$)figure.4a) reports the mismatch Δk for SH generation, which never vanishes in the FF range $[1300 - 2000]nm$. At the output of the crystal we note a broadband extraordinary SH and ordinary TH, as well as the presence of some TH spikes given by quasi phase matching of higher order spatial harmonics of the grating (fig. 3Input (dashed curves) and output (solid curves) power spectrum after propagation in a PPMgOLN crystal. Red and blue curves represent extraordinary and ordinary polarized spectra, respectively. Power spectrum is shown both as a function of frequency (a) and of wavelength (b)figure.3). The TH spikes at $540nm$ and $470nm$ corresponds to a broadband type-II sum frequency generation ($o + e \rightarrow o$) matched by fifth (V) and seventh (VII) order QPM, respectively. Indeed, fig. 4a) Phase-matching curve for type I SHG interaction in a PPMg0LN crystal. b) Level curves of sum frequency wavelength ($\lambda_3 = \lambda_1 + \lambda_2$) and of mismatch $\Delta k = 0$ (thick blue curves) for V-order (superimposed to $\lambda = 540nm$) and VII-order QPM (superimposed to $\lambda = 470nm$)figure.4b) reports the sum frequency wavelengths ($\lambda_3 = \lambda_1 + \lambda_2$) and the matching curve $\Delta k_{oeo} = k_3 - k_2 - k_1 = 0$ as a function of wavelengths $\lambda_{1,2}$; the V-order and VII-order matching curves are practically superimposed to sum frequency $\lambda = 540nm$ and $\lambda = 470nm$.

4. Conclusions

We derived the propagation equations for electric fields in anisotropic, dispersive, quadratic nonlinear media. Our approach enable us to simulate unidirectional electromagnetic propagation in uniaxial quadratic media with modest computational effort, order of magnitudes less than the numerical solution of full Maxwell equations. We have exploited this model to simulate recently observed femtosecond single-cycle multiterahertz transients in gallium selenide and to predict harmonic generation and spectral broadening in the visible and mid-infrared in lithium niobate.

Appendix

Equations (22equation.2.22) posses the following conserved quantity, proportional to the total intensity of the field:

$$I = \int \Big[n_x(\omega) |\hat{E}_x(\omega)|^2 + n_y(\omega) |\hat{E}_y(\omega)|^2 \Big] d\omega \tag{23}$$

where the integration is performed from $-\infty$ to $+\infty$, and $n(\omega)$ is assumed to be real (lossless medium).

We have:

$$\begin{aligned}
\frac{dI}{dz} &= \sum_{m=x,y} \int n_m(\omega) \Big[\frac{\partial \hat{E}_m}{\partial z} \hat{E}_m^* + \frac{\partial \hat{E}_m^*}{\partial z} \hat{E}_m \Big] d\omega \\
&= \frac{-i\omega}{c} \Big[2d_1 \int\int \omega \hat{E}_x(\omega') \hat{E}_y(\omega - \omega') \hat{E}_x^*(\omega) d\omega d\omega' \\
&+ d_2 \int\int \omega \hat{E}_y(\omega') \hat{E}_y(\omega - \omega') \hat{E}_x^*(\omega) d\omega d\omega' \\
&+ d_1 \int\int \omega \hat{E}_x(\omega') \hat{E}_x(\omega - \omega') \hat{E}_y^*(\omega) d\omega d\omega' \\
&+ 2d_2 \int\int \omega \hat{E}_x(\omega') \hat{E}_y(\omega - \omega') \hat{E}_y^*(\omega) d\omega d\omega' - c.c. \Big] \\
&= \frac{-i\omega}{c} [J_1 - J_2]
\end{aligned}$$

By exploiting the Hermiticity of $\hat{E}$ and by the change of variables ($\omega \to -\omega$, $\omega' \to -\omega'$) in the integrals J_1, we obtain $J_1 = -J_2$, so that:

$$\begin{aligned}
\frac{dI}{dz} &= \frac{2}{c} \Big\{ 2d_1 \int [i\omega \hat{E}_x(\omega)]^* \Big[\int \hat{E}_x(\omega') \hat{E}_y(\omega - \omega') d\omega' \Big] d\omega \\
&+ d_2 \int [i\omega \hat{E}_x(\omega)]^* \Big[\int \hat{E}_y(\omega') \hat{E}_y(\omega - \omega') d\omega' \Big] d\omega \\
&+ d_1 \int [i\omega \hat{E}_y(\omega)]^* \Big[\int \hat{E}_x(\omega') \hat{E}_x(\omega - \omega') d\omega' \Big] d\omega \\
&+ 2d_2 \int [i\omega \hat{E}_y(\omega)]^* \Big[\int \hat{E}_x(\omega') \hat{E}_y(\omega - \omega') d\omega' \Big] d\omega \Big\}
\end{aligned}$$

By exploiting Parseval's theorem (i.e. conservation of scalar product), we can write the integrals in time domain, and considering that the fields must vanish at infinity we have:

$$\begin{aligned}
\frac{dI}{dz} &= \frac{2}{c} \Big[2d_1 \int \frac{\partial E_x}{\partial t} E_x E_y dt + d_2 \int \frac{\partial E_x}{\partial t} E_y^2 dt \\
&+ d_1 \int \frac{\partial E_y}{\partial t} E_x^2 dt + 2d_2 \int \frac{\partial E_y}{\partial t} E_x E_y dt \Big] = 0
\end{aligned}$$

where in the last step we have integrated by parts the second and third terms.

References

1. R. Huber, F. Tauser, A. Brodschelm, M. Bichler, G. Abstreiter, and A. Leitenstorfer , "How many-particle interactions develop after ultrafast excitation of an electronhole plasma," Nature **414**, 286-289 (2001).
2. G. Gunter, A. A. Anappara, J. Hees, A. Sell, G. Biasiol, L. Sorba, S. De Liberato, C. Ciuti, A. Tredicucci, A. Leitenstorfer, and R. Huber , "Sub-cycle switch-on of ultrastrong lightmatter interaction," Nature **458**, 178-181 (2009).
3. T. Brabec and F. Krausz, "Intense few-cycle laser fields: Frontiers of nonlinear optics," Rev. Mod. Phys. **72**, 545-591 (2000).
4. C. Chudoba, E. Nibbering, and T. Elsaesser, "Site-specific excited-state solute-solvent interactions probed by femtosecond vibrational spectroscopy," Phys. Rev. Lett., **81**, 3010-3013 (1998).
5. E.J. Heilweil, "Ultrafast glimpses at water and ice," Science **283**, 1467-1468 (1999).
6. S. Woutersen, U. Emmerichs, and H.J. Bakker, "Femtosecond mid-IR pump probe spectroscopy of liquid water: evidence for a two-component structure," Science **278**, 658-660 (1997).
7. G. Cerullo and S. De Silvestri, "Ultrafast Optical Parametric Amplifiers," Rev. Sci. Instrum. **74**, 1-18 (2003).
8. D. Polli, L. Luer and G. Cerullo, "High-time-resolution pump-probe system with broadband detection for the study of time-domain vibrational dynamics," Rev. Sci. Instrum. **78**, 1031081-1031089 (2007).
9. C. Manzoni, G. Cerullo, and S. De Silvestri, "Ultrabroadband self-phase-stabilized pulses by difference-frequency generation," Opt. Lett. **29**, 2668-2670 (2004).
10. F. Junginger, A. Sell, O. Schubert, B. Mayer, D. Brida, M. Marangoni, G. Cerullo, A. Leitenstorfer, and R. Huber "Single-cycle multiterahertz transients with peak fields above 10 MV/cm," Opt. Lett. **35**, 2645-2647 (2010).
11. D. Brida, C. Manzoni, G. Cirmi, M. Marangoni, S. Bonora, P. Villoresi, S. De Silvestri, and G. Cerullo "Few-optical-cycle pulses tunable from the mid-infrared by optical parametric amplifiers," J. Opt. **12**, 013001–0130013

(2010).

12. R. W. Boyd, *Nonlinear Optics*, (Academic Press, 2003), 2nd ed.
13. P. Kinsler and G. H. C. New, "Few-cycle pulse propagation," Phys. Rev. A **67**, 023813 (2003).
14. J. Moses and F. W. Wise, "Controllable Self-Steepening of Ultrashort Pulses in Quadratic Nonlinear Media," Phys. Rev. Lett. **97**, 073903 (2006).
15. M. Geissler, G. Tempea, A. Scrinzi, M. Schnurer, F. Krausz, and T. Brabec, "Light propagation in field-ionizing media: extreme nonlinear optics," Phys. Rev. Lett. **83**, 2930-2933 (1999).
16. A. V. Housakou and J. Herrmnann, "Supercontinuum generation of higher-order solitons by fission in photonic crystal fibers," Phys. Rev. Lett., vol. **87**, 203901 (2001).
17. M. Kolesik, J. V. Moloney and M. Mlejnek, "Unidirectional optical pulse propagation equation," Phys. Rev. Lett. **89**, 283902 (2002).
18. M. Kolesik and J. V. Moloney, "Nonlinear optical pulse propagation simulation: From Maxwell's to unidirectional equations," Phys. Rev. E **70**, 036604 (2004).
19. G. Genty, P. Kinsler, B. Kibler and J.M. Dudley, "Nonlinear envelope equation modeling of sub-cycle dynamics and harmonic generation in nonlinear waveguides," Opt. Express **15** 5382-5387 (2007).
20. P. Kinsler, S. B. P. Radnor, and G. H. C. New, "Theory of directional pulse propagation," Phys. Rev. A **72**, 063807 (2005).
21. P. Kinsler, "Optical pulse propagation with minimal approximations," Phys. Rev. A **81** 013819 (2010).
22. A. Kumar, "Ultrashort pulse propagation in a cubic medium including the Raman effect," Phys. Rev. A **81** 013807 (2010).
23. M. Conforti, F. Baronio, and C. De Angelis, "Nonlinear envelope equation for broadband optical pulses in quadratic media," Phys. Rev. A **81** 053841 (2010).
24. M. Conforti, F. Baronio, and C. De Angelis, "Ultra-broadband optical phenomena in quadratic nonlinear media," IEEE Photonics J. **2**, 600-610 (2010).
25. L. D. Landau and E. M. Lifshitz, "Electrodynamics of continuous media",

Pergamon, New York (1984).

26. J. E. Midwinter and J. Warner, "The effects of phase matching method and of uniaxial crystal symmetry on the polar distribution of second-order nonlinear optical polarization", Brit. J. Appl. Phys. **161**, 1135-1142 (1965).
27. D. N. Nikogosyan, *Nonlinear Optical Crystals: A Complete Survey*, Springer (2005)
28. M. Conforti, F. Baronio, A. Degasperis, and S. Wabnitz, "Parametric frequency conversion of short optical pulses controlled by a CW background", Opt. Express **15**, 12246-12251 (2007).
29. F. Baronio, M. Conforti, A. Degasperis, and S. Wabnitz, "Three-wave trapponic solitons for tunable high-repetition rate pulse train generation", IEEE J. Quant. Electron. **44**, 542-546 (2008).
30. N. E. Yu, J. H. Ro, M. Cha, S. Kurimura, and T. Taira, "Broadband quasi-phase-matched second-harmonic generation in MgO-doped periodically poled $LiNbO_3$ at the communications band", Opt. Lett. **27**, 1046-1048 (2002).
31. N. E. Yu, S. Kurimura, K. Kitamura, J. H. Ro, M. Cha, S. Ashihara, T. Shimura, K. Kuroda, and T. Taira, "Efficient frequency doubling of a femtosecond pulse with simultaneous group-velocity matching and quasi phase matching in periodically poled, MgO-doped lithium niobate", Appl. Phys. Lett. **82**, 3388-3390 (2003).

Figure Captions

- Figure 1: Generation of single cycle idler pulse by parametric mixing of pump and signal waves centered at 1.18 and 1.28 μm, respectively. $I_p = 25GW/cm^2$, $I_s = 40GW/cm^2$, L=140μm. a) Input (dashed curves) and output (solid curves) power spectrum of extraordinary wave E_x (red curves) and ordinary wave E_y (blue curves). b) Power spectrum of ordinary output THz component. c) Single cycle THz transients obtained by filtering E_y in [1-100] THz range. Dashed curve, in phase pump-signal input; solid curve, phase difference $3/4\pi$.

- Figure 2: Evolution of the total power spectrum (dB). The initial pulse has gaussian shape and the parameters are $T = 100fs$, $\lambda = 1550nm$, $I = 60GW/cm^2$, $\Lambda_{QPM} = 19.55\mu m$, $\theta = \phi = \pi/2$.

- Figure 3: Input (dashed curves) and output (solid curves) power spectrum after propagation in a PPMgOLN crystal. Red and blue curves represent extraordinary and ordinary polarized spectra, respectively. Power spectrum is shown both as a function of frequency (a) and of wavelength (b).

- Figure 4: a) Phase-matching curve for type I SHG interaction in a PPMg0LN crystal. b) Level curves of sum frequency wavelength ($\lambda_3 = \lambda_1 + \lambda_2$) and of mismatch $\Delta k = 0$ (thick blue curves) for V-order (superimposed to $\lambda = 540nm$) and VII-order QPM (superimposed to $\lambda = 470nm$).

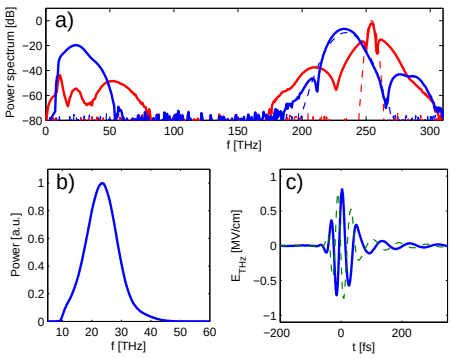

Fig. 1. Generation of single cycle idler pulse by parametric mixing of pump and signal waves centered at 1.18 and 1.28 μm, respectively. $I_p = 25GW/cm^2$, $I_s = 40GW/cm^2$, L=140μm. a) Input (dashed curves) and output (solid curves) power spectrum of extraordinary wave E_x (red curves) and ordinary wave E_y (blue curves). b) Power spectrum of ordinary output THz component. c) Single cycle THz transients obtained by filtering E_y in [1-100] THz range. Dashed curve, in phase pump-signal input; solid curve, phase difference $3/4\pi$.

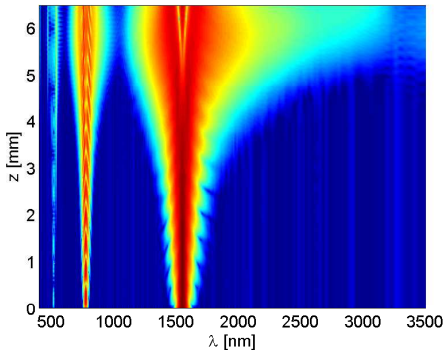

Fig. 2. Evolution of the total power spectrum (dB). The initial pulse has gaussian shape and the parameters are $T = 100fs$, $\lambda = 1550nm$, $I = 60GW/cm^2$, $\Lambda_{QPM} = 19.55\mu m$, $\theta = \phi = \pi/2$

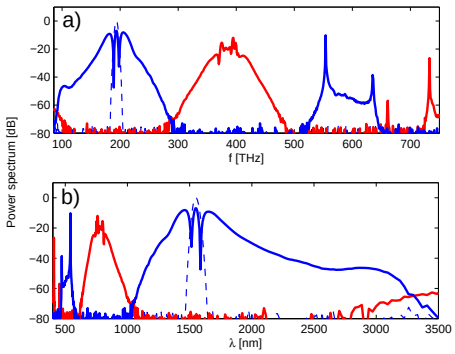

Fig. 3. Input (dashed curves) and output (solid curves) power spectrum after propagation in a PPMgOLN crystal. Red and blue curves represent extraordinary and ordinary polarized spectra, respectively. Power spectrum is shown both as a function of frequency (a) and of wavelength (b).

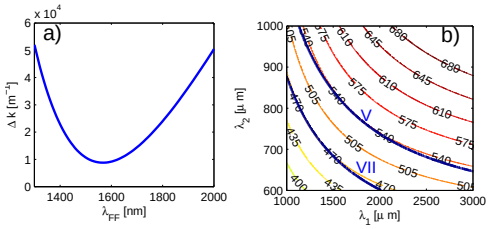

Fig. 4. a) Phase-matching curve for type I SHG interaction in a PPMg0LN crystal. b) Level curves of sum frequency wavelength ($\lambda_3 = \lambda_1 + \lambda_2$) and of mismatch $\Delta k = 0$ (thick blue curves) for V-order (superimposed to $\lambda = 540nm$) and VII-order QPM (superimposed to $\lambda = 470nm$).

Crystal	d_1 (eeo, eoe, oee)	d_2 (ooe, oeo, eoo)
GaSe	$d_{22}\cos^2\theta\cos 3\phi$	$d_{22}\cos\theta\sin 3\phi$
MgO:LN	$d_{22}\cos^2\theta\cos 3\phi$	$d_{31}\sin\theta - d_{22}\cos\theta\sin 3\phi$

Table 1. Effective Nonlinear Coefficients. As to GaSe, $d_{22} = 54pm/V$; as to MgOLN $d_{22} = 0$, $d_{31} = 4.5pm/V$.